A Multiinput Bridgeless Resonant AC–DC Converter for Electromagnetic Energy Harvesting

Yichao Tang, *Student Member, IEEE*, and Alireza Khaligh, *Senior Member, IEEE*

***Abstract*—Flapping electromagnetic-reed generators are investigated to harvest wind energy, even at low cutoff wind speeds. Power electronic interfaces are intended to address ac–dc conversion and power conditioning for single- or multiple-channel systems. However, the generated voltage of each generator reed at low wind speed is usually below the threshold voltage of power electronic semiconductor devices, increasing the difficulty and inefficiency of rectification, particularly at relatively low output powers. This paper proposes a multiinput bridgeless resonant ac–dc converter to achieve ac–dc conversion, step-up voltage and match optimal impedance for a multichannel electromagnetic energy harvesting system. Alternating voltage of each generator is stepped up through the switching *LC* network and then rectified by a freewheeling diode. Its resonant operation enhances efficiency and enables miniaturization through high frequency switching. The optimal electrical impedance can be adjusted through resonance impedance matching and pulse-frequency-modulation control. A 5 cm × 3 cm, six-input standalone prototype is fabricated to address power conditioning for a six-channel wind panel.**

***Index Terms*—Ac–dc conversion, electromagnetic energy harvesting, multiinput converter, resonant converter, wind energy.**

I. Introduction

WIND energy is considered as one of the most promising alternative sources. Flapping electromagnetic-reed (EMR) generators, suitable to energize standalone small-size and low-power electrical loads, such as light poles and wireless sensors, can harvest energy from wind-induced vibration [1]. The EMR generators, such as the wind energy harvesting cell proposed in [2], are suitable for virtually any wind conditions including turbulent wind found in many real-world settings [3]–[5]. Power electronic interfaces (PEI) are required to condition the output power of energy harvesters and effectively deliver power to the loads [6]–[14], as shown in Fig. 1 (a). Power density and efficiency at low power conversion are important performance metrics of power converters for low-speed wind energy harvesting. One of the main challenges toward fabricating efficient converters for EMR generators is the efficient rectification of low-amplitude generator voltages [15], [16]. Due to large voltage drop of diodes, the conventional diode-bridge topologies are inefficient and in some cases impractical for low-voltage and low-power energy harvesting applications.

Manuscript received November 15, 2014; revised January 13, 2015 and March 31, 2015; accepted April 21, 2015. Date of publication April 27, 2015; date of current version November 16, 2015. This work was supported in part by the Maryland Industrial Partnerships Program. Recommended for publication by Associate Editor R. Redl.

The authors are with the Power Electronics, Energy Harvesting and Renewable Energies Laboratory, Electrical and Computer Engineering Department, Institute for Systems Research, University of Maryland, College Park, 20742 MD USA (e-mail: ychtang1986@gmail.com; khaligh@ece.umd.edu).

Color versions of one or more of the figures in this paper are available online at http://ieeexplore.ieee.org.

Digital Object Identifier 10.1109/TPEL.2015.2426700

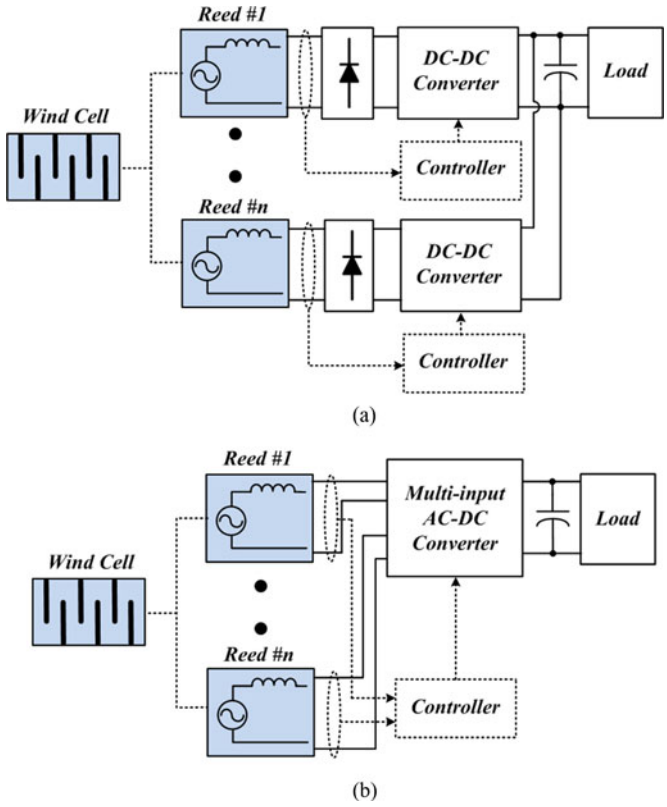

Fig. 1. Multichannel EMR generators and PEI system: (a) conventional PEI and (b) proposed multiinput PEI.

The majority of efforts toward efficient rectification of low-voltage irregular outputs of EMR generators has focused on replacing the conventional p-n junction diodes with modified MOSFET connection, including diode-connected MOSFETs [17], gate cross-coupled MOSFETs [18], and active diodes [19]. These technologies reduce the forward voltage-drop of diodes through different connections of MOSFET terminals. However, such rectifiers suffer from losses caused either by gate threshold voltage or turn-on resistance of MOSFET. Moreover, these passive rectifiers require a second stage to regulate electrical impedance, inherently reducing the efficiency.

Researchers have studied single-stage bridgeless ac–dc switching converters, including H-bridge converter [20], ac–dc boost converter, ac–dc buck-boost converter [21] and ac–dc switch-inductor boost converter [22]. These topologies provide ac–dc conversion and impedance regulation through either using bidirectional transistors and split capacitors, or paralleling dc–dc converters. However, they suffer from drawbacks in terms of inefficient hard switching, asymmetrical operation and complicated high-side gate drive. Soft-switching converters are

considered for efficient rectification at high switching frequencies [23], [24]. Majority of investigations on soft-switching converters focus on modification of hard-switching converters, referred as quasi-resonant converters. They utilize auxiliary *LC* resonant circuits to primarily shape the current and voltage of main transistors during the turn-on and turn-off of the switching components [25], [26]. However, the auxiliary resonant circuits result in additional footprint, switching losses and conduction losses. Resonant converters, such as synchronized switch harvesting on inductor converters [27]–[30], utilize passive resonant networks as low impedance branches across transistors. They eliminate the switching losses without additional bulky components. However, a postpositioned bridge rectification stage, such as a dual-stage resonant boost converter, is required for ac–dc conversion [31].

In this paper, a new multiinput bridgeless resonant ac–dc converter, illustrated in Fig. 1 (b), is proposed to efficiently convert low-amplitude alternative voltages of multiple EMR generators into a regulated dc output voltage. The topology is capable of interfacing multiple, independent, alternating, input sources without using a diode bridge. Very-low-amplitude voltages can be stepped up to a relatively high voltage. Larger number of input sources results even in higher output voltage. The resonance nature of operation eliminates the switching losses, and allows high frequency switching. It also enables miniaturization through using substantially smaller capacitive and magnetic components. The multiinput converter uses the self-inductance of input sources, and only utilizes one magnetic component and one diode. Furthermore, this topology reduces the voltage stress on power transistors. In summary, the proposed topology has superiorities in terms of: 1) capability of interfacing and conditioning the output power of multiple EMR generators; 2) no need for inefficient diode bridge; 3) small number and value of passive components; 4) high voltage gain at 0.5 switching duty cycle; 5) resonant lossless switching; 6) relatively low stress on transistors; and 7) simple gate drive.

This paper is organized as follows. Section II presents the operation principle of an EMR generator and the modeling of a breeze energy system. Soft-switching operation modes, steady-state analyses and optimal impedance matching are investigated in Section III. The design specification for a six-input converter and experimental results are presented in Section IV. Finally, Section V concludes the paper.

II. Multiinput Resonant AC–DC Converter

A. EMR Generator Model

According to the general model of an electromagnetic system, one EMR generator can be modeled as a bipolar time-varying electromotive force (EMF or open-circuit voltage, $v_{\rm emf}$) connected in series with an inner resistance (coil resistance, $r_{\rm EMR}$) and a self-inductance (coil inductance, $L_{\rm EMR}$) [32]. Both the equivalent mechanical and electrical models are presented in Fig. 2. The PEI needs to be designed to achieve: 1) rectification, 2) voltage step-up, 3) impedance matching, and 4) high efficiency operation across wide output voltages.

Conventionally, the EMR generators are interfaced with diode bridges for rectification [6]. Due to the rectification, the equivalent open-circuit voltage ($|v_{\rm emf}|$) is equal to the absolute value

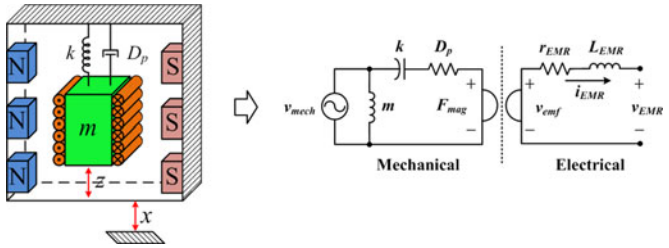

Fig. 2. Equivalent circuit of one EMR generator ($v_{\rm mech}$: mechanical velocity; *m*: proof mass; *k*: spring stiffness; D_p: mechanical damping; $F_{\rm mag}$: magnetic force; $v_{\rm emf}$: EMF; $r_{\rm EMR}$: coil resistance; $L_{\rm EMR}$: self-inductance; $i_{\rm EMR}$: reed terminal current; $v_{\rm EMR}$: reed terminal voltage).

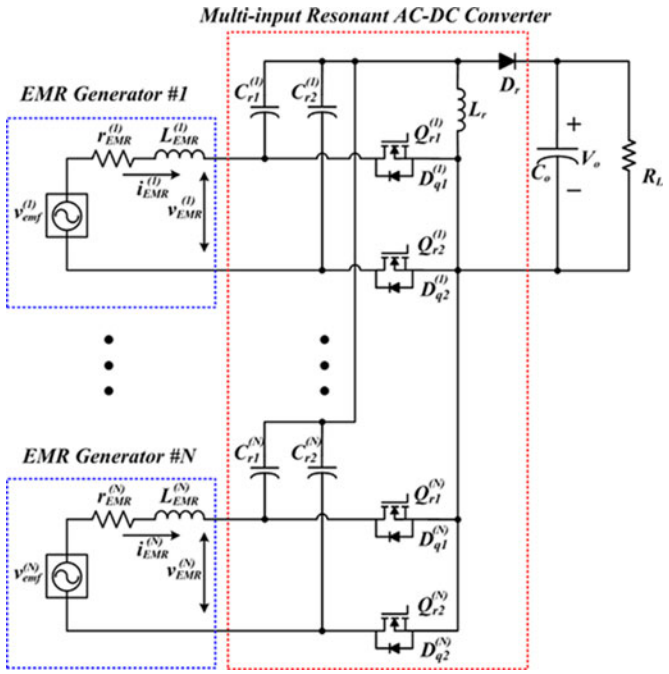

Fig. 3. Illustrative scheme of the proposed multiinput converter ($v^{(i)}_{\rm emf}$: EMF of #i reed; $r^{(i)}{}_{\rm EMR}$: coil resistance; $L^{(i)}{}_{\rm EMR}$: self-inductance; $i^{(i)}{}_{\rm EMR}$: reed terminal current; $v^{(i)}_{\rm EMR}$: reed terminal voltage; $C^{(i)}{}_{r1} = C^{(i)}{}_{r2}$: resonant capacitors; L_r: resonant inductor; $Q^{(i)}{}_{r1}$, $Q^{(i)}{}_{r2}$: MOSFETs; D_r: output diode; C_o: output capacitor).

of EMF. First, since the load is connected in series with the reed, the load root-mean-square (RMS) voltage is lower than RMS value of generator EMF. However, in most of cases, a load voltage higher than EMF is required (i.e., for battery charging). As a result, a switching power converter capable of stepping up the EMF is necessary. Second, in order to extract the maximum power from a source, the equivalent input impedance ($Z_{\rm in}$) of the circuit should be set equal to the optimal impedance ($Z_{\rm opt}$) for impedance matching [33]. However, with a wide range of load (R_L), it is difficult and impractical to adjust the input impedance to the optimal value by using a diode bridge. A switching power converter should be used to adjust the impedance (Z_r) and regulate the input impedance ($Z_{\rm in}$) for optimal impedance matching.

B. Circuit Description

Fig. 3 illustrates the proposed multiinput single-stage bridgeless resonant ac–dc converter. The topology is capable of

operating with multiple inductive sources. Each inductive source, in this case EMR generator, is numbered with $i = 1, 2, \ldots, N$. The multiinput circuit is formed by one resonant inductor, one diode and multiple MOSFET-capacitor bridges. Each input source is connected to two MOSFET-capacitor bridges ($Q^{(i)}{}_{r1}$, $C^{(i)}{}_{r1}$ and $Q^{(i)}{}_{r2}$, $C^{(i)}{}_{r2}$), which share a resonant inductor and a diode.

The resonant inductor (L_r) is tuned with resonant capacitors ($C^{(i)}{}_{r1}$ and $C^{(i)}{}_{r2}$) to resonate at the resonant frequency (f_r) near the switching frequency (f_s). Ideally, the resonant components (L_r, $C^{(i)}{}_{r1}$ and $C^{(i)}{}_{r2}$) present a lossless low drain-to-source impedance branch across MOSFETs near f_s. The *LC* network amplifies the EMF. $C^{(i)}{}_{r1}$ and $C^{(i)}{}_{r2}$ are in parallel with MOSFETs and the diode to ensure ZVS at turning-on and turning-off. Switching losses are eliminated through the oscillating voltage and current, while the input energy is stored and released to the load through the active *LC* network. Furthermore, the tuned networks eliminate overvoltage spikes as well as diode reverse recovery issues while simultaneously maintaining low peak voltage stresses on MOSFETs.

MOSFETs ($Q^{(i)}{}_{r1}$ and $Q^{(i)}{}_{r2}$) are actively turned on and off with duty cycle close to 0.5 in order to generate drain-to-source pulse voltage ($v^{(i)}{}_{\rm ds1}$ and $v^{(i)}{}_{\rm ds2}$) at the input of *LC* network. The amplitude of drain-to-source pulse voltage is higher than $v_{\rm emf}$ due to the energy stored in $L^{(i)}{}_{\rm EMR}$. The fundamental component of $v^{(i)}{}_{\rm ds1}$ and $v^{(i)}{}_{\rm ds2}$ pass through the *LC* network and generate an amplified oscillating voltage near f_s across the rectifier diode D_r. ZVS and ZCS operation of $Q^{(i)}{}_{r1}$ and $Q^{(i)}{}_{r2}$ provide energy recovery to drain-to-source MOSFET parasitic capacitor ($C_{\rm ds}$), which in turn increases the efficiency. The drain-to-source overvoltage spike is eliminated; thereby no snubber circuit is required. The output diode (D_r) rectifies the amplified oscillating voltage after the tuned network into a dc output voltage. It generates freewheeling path for the resonant inductor current as well as charging path for the resonant capacitors.

C. Operation Mode Analyses

In a switching cycle, one EMR generator can be assumed as a current source if the generator has a large self-inductance. In this case, for simplicity of analysis, each EMR generator is assumed as a current source ($I^{(i)}{}_{\rm in}$) during a switching period. In a mechanical vibration cycle, $I^{(i)}{}_{\rm in}$ is positive at positive half cycle and is negative at negative half cycle. There are three switching submodes during one switching cycle at either positive half cycle or negative half cycle. For simplicity, the switching submodes of a dual-input topology with a positive input and a negative input, as illustrated in Fig. 4 (a), are presented in steady state. The analyses can be analogously extended to the multiinput topology. For a positive input ($I^{(1)}{}_{\rm in}$), $Q^{(1)}{}_{r2}$ is conducting in all submodes while $Q^{(1)}{}_{r1}$ is switching; for a negative input ($I^{(2)}{}_{\rm in}$), $Q^{(2)}{}_{r1}$ is conducting in all submodes while $Q^{(2)}{}_{r2}$ is switching. Therefore, the rectification of each bipolar source is achieved by conducting $Q^{(i)}{}_{r2}$ while switching $Q^{(i)}{}_{r1}$ at positive input cycle; or conducting $Q^{(i)}{}_{r1}$ while switching $Q^{(i)}{}_{r2}$ at negative input cycle.

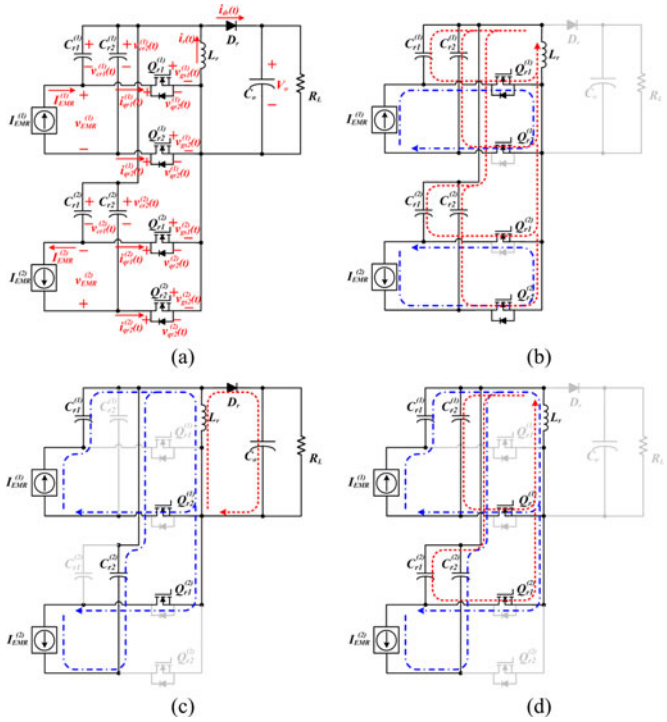

Fig. 4. (a) Simplified topology of dual-input resonant converter with a positive input and a negative input. (b)–(d) Switching submodes during a switching cycle.

The simulation waveforms of reed #1 during one switching cycle are demonstrated in Fig. 5. The switching frequency is close to the resonant frequency (f_r) of $L_r C_{r1} C_{r2}$ network, and the switching duty cycle is close to 0.5. Relative to the resonant capacitors, C_o has very small impedance at f_s, thereby it acts as a voltage source and can be considered as a constant value, $V_{\rm o}$. The capacitances $C^{(i)}{}_{r1}$ and $C^{(i)}{}_{r2} (i = 1, 2)$ are set equal to C_r for the impedance matching.

At t_0: (circuit initial state) It is assumed that $I^{(1)}{}_{\rm EMR}$ and $I^{(2)}{}_{\rm EMR}$ have initial values. $v^{(1)}{}_{\rm cr1}$, $v^{(1)}{}_{\rm cr2}$, $v^{(2)}{}_{\rm cr1}$ and $v^{(2)}{}_{\rm cr2}$ have the same negative initial values, $v_{\rm cr1}(t_0)$. $Q^{(1)}{}_{r1}$ and $Q^{(2)}{}_{r2}$ are both off before t_0.

Mode I ($t_0 \sim t_1$): At t_0, as shown in Fig. 4 (b), body diodes of $Q^{(1)}{}_{r1}$ and $Q^{(2)}{}_{r2}$ are turned on at zero voltage [$v^{(1)}{}_{qr1}(t_0)$ and $v^{(2)}{}_{qr2}(t_0)$] (equal to $v^{(1)}{}_{\rm cr2} - v^{(1)}{}_{\rm cr1}$). As soon as the currents through body diodes reduce to zero, $Q^{(1)}{}_{r1}$ and $Q_r^{(2)}{}_2$ are turned on at zero voltage [$v^{(1)}{}_{qr1}(t_0)$ and $v^{(2)}{}_{qr2}(t_0)$] (equal to $v^{(1)}{}_{\rm cr2} - v^{(1)}{}_{\rm cr1}$) and zero current [$i^{(1)}{}_{qr1}(t_0)$ and $i^{(2)}{}_{qr2}(t_0)$]. The self-inductances of reeds start to get charged by the input EMFs, thereby $I^{(1)}{}_{\rm EMR}$ and $I^{(2)}{}_{\rm EMR}$ increase linearly. $C^{(1)}{}_{r1}$, $C^{(1)}{}_{r2}$, $C^{(2)}{}_{r1}$ and $C^{(2)}{}_{r2}$ begin to resonate with L_r at f_r. $v^{(1)}{}_{\rm cr1}$, $v^{(1)}{}_{\rm cr2}$, $v^{(2)}{}_{\rm cr1}$ and $v^{(2)}{}_{\rm cr2}$ are equal and increase sinusoidally until they are equal to V_o at t_1. The governing equations in terms of $v^{(i)}{}_{\rm cr1}$, $v^{(i)}_{cr2}$ and i_r are

$$\begin{cases} \dfrac{\partial i_r(t)}{\partial t} = -\dfrac{v^{(i)}_{cr1}(t)}{L_r} = -\dfrac{v^{(i)}_{cr2}(t)}{L_r} & (1) \\ \dfrac{\partial v^{(i)}_{cr1}(t)}{\partial t} = \dfrac{\partial v^{(i)}_{cr2}(t)}{\partial t} = \dfrac{i_r(t)}{2NC_r} & (2) \end{cases}$$

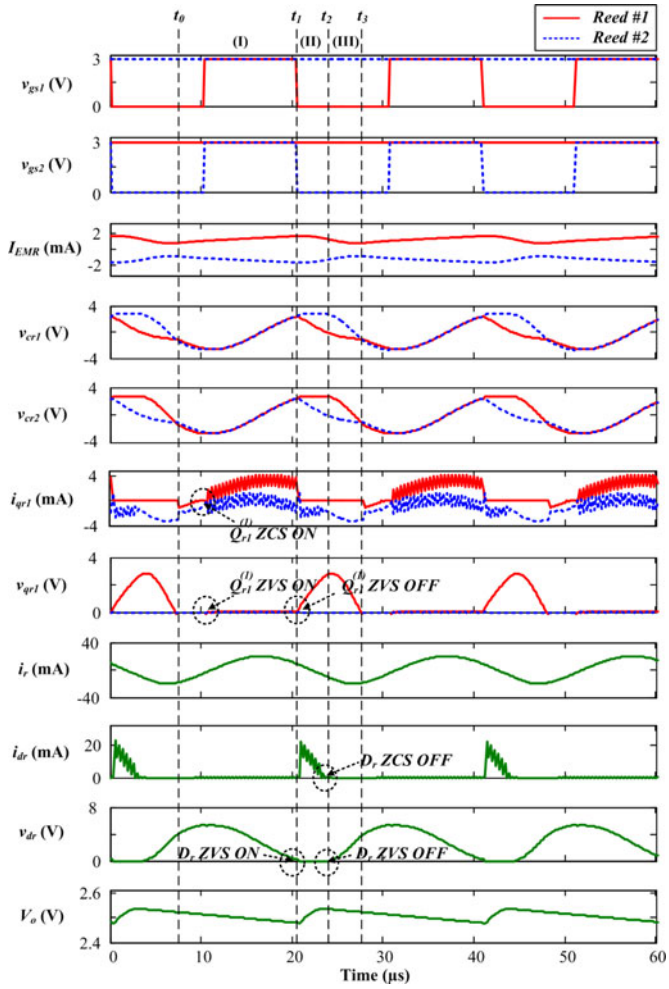

Fig. 5. Simulation waveforms of reed #1 during a switching cycle.

where $N = 2$ is the number of input sources. Hence, the transient state of i_r and $v^{(i)}{}_{\rm cr1}$ can be expressed as

$$\begin{cases} i_r(t) = i_r(t_0)\cos\omega_r(t-t_0) - \dfrac{v^{(i)}_{cr1}(t_0)}{Z_r}\sin\omega_r(t-t_0) & (3) \\ v^{(i)}_{\rm cr1}(t) = v^{(i)}_{\rm cr2}(t) = v^{(i)}_{\rm cr1}(t_0)\cos\omega_r(t-t_0) \\ \quad + i_r(t_0)Z_r\sin\omega_r(t-t_0) & (4) \end{cases}$$

where $\omega_r = (2NL_rC_r)^{-1/2}$ is the angular resonance frequency of LC network; and $Z_r = (L_r/2NC_r)^{1/2}$ is the characteristic impedance of LC network. Assuming $i_r(t_0)$ is very small, the first component of $i_r(t)$ and the second component of $v^{-(i)}_{\rm cr1}(t)$ can be neglected.

Mode II ($t_1 \sim t_2$): At t_1, $Q^{(1)}{}_{r1}$ and $Q^{(2)}{}_{r2}$ are turned off at zero voltage [$v^{(1)}{}_{qr1}(t_1)$ and $v^{(2)}{}_{qr2}(t_1)$], as depicted in Fig. 4 (c). The energy stored in the reed self-inductance begins to be transferred to L_r. D_r turns on at zero voltage [$v_{\rm dr}(t_1)$], allowing the current (equal to $I^{(1)}{}_{\rm EMR} + I^{(2)}{}_{\rm EMR} + i_r$) to freewheel through D_r. i_r decreases linearly due to V_o across L_r. In this mode, $v^{(1)}{}_{\rm cr1}$ and $v^{(2)}{}_{\rm cr2}$ decrease; however, $v^{(1)}{}_{\rm cr2}$ and $v^{(2)}{}_{\rm cr1}$ remain equal to V_o. The governing equations are

$$\begin{cases} \dfrac{\partial i_r(t)}{\partial t} = -\dfrac{V_o}{L_r} & (5) \\ \dfrac{\partial v^{(1)}_{\rm cr1}(t)}{\partial t} = -\dfrac{I^{(1)}_{\rm EMR}}{C_r} & (6) \\ \dfrac{\partial v^{(2)}_{\rm cr2}(t)}{\partial t} = -\dfrac{I^{(2)}_{\rm EMR}}{C_r}. & (7) \end{cases}$$

$v^{(1)}{}_{\rm cr1}$ and $v^{(2)}{}_{\rm cr2}$ decrease linearly from their boundary condition $v^{(1)}{}_{\rm cr1}(t_1) = v^{(2)}{}_{\rm cr2}(t_1) = V_o$, yielding

$$\begin{cases} i_r(t) = -\dfrac{V_o}{L_r}(t-t_1) + i_r(t_1) & (8) \\ v^{(1)}_{\rm cr1}(t) = -\dfrac{I^{(1)}_{\rm EMR}}{C_r}(t-t_1) + V_o & (9) \\ v^{(2)}_{\rm cr2}(t) = -\dfrac{I^{(2)}_{\rm EMR}}{C_r}(t-t_1) + V_o & (10) \\ v^{(1)}_{\rm cr2}(t) = v^{(2)}_{\rm cr1}(t) = V_o. & (11) \end{cases}$$

Mode III ($t_2 \sim t_3$): At t_2, $i_{\rm dr}$ drops to zero, leaving no current to freewheel through D_r. D_r turns off at both zero voltage [$v_{\rm dr}(t_2)$] and zero current [$i_{\rm dr}(t_2)$] at t_2. $C^{(1)}{}_{r2}$, $C^{(2)}{}_{r1}$, and L_r begin to resonate, until $v^{(1)}{}_{\rm cr2}$ and $v^{(2)}{}_{\rm cr1}$ are respectively equal to $v^{(1)}{}_{\rm cr1}$ and $v^{(2)}{}_{\rm cr2}$ at t_3. The governing equations of Mode III can be represented as

$$\begin{cases} \dfrac{\partial i_r(t)}{\partial t} = -\dfrac{v^{(1)}_{\rm cr2}(t)}{L_r} = -\dfrac{v^{(2)}_{\rm cr1}(t)}{L_r} & (12) \\ \dfrac{\partial v^{(1)}_{\rm cr2}(t)}{\partial t} = \dfrac{\partial v^{(2)}_{\rm cr1}(t)}{\partial t} = \dfrac{\sum_{i=1}^{N} I^{(i)}_{\rm EMR} + i_r(t)}{NC_r}. & (13) \end{cases}$$

The governing equations of $v^{(1)}{}_{\rm cr1}$ and $v^{(2)}{}_{\rm cr2}$ are similar to those in Mode II. By applying boundary conditions $v^{(1)}{}_{\rm cr2}(t_2) = v^{(2)}{}_{\rm cr1}(t_2) = V_o$ and $i_r(t_2) = -I^{(1)}{}_{\rm EMR} - I^{(2)}{}_{\rm EMR}$, i_r, $v^{(1)}{}_{\rm cr2}$ and $v^{(2)}{}_{\rm cr1}$ can be presented as

$$\begin{cases} i_r(t) = -\sum_{i=1}^{N} I^{(i)}_{\rm EMR} - \dfrac{V_o}{\sqrt{2}Z_r}\sin\sqrt{2}\omega_r(t-t_2) & (14) \\ v^{(1)}_{\rm cr2}(t) = v^{(2)}_{\rm cr1}(t) = V_o\cos\sqrt{2}\omega_r(t-t_2). & (15) \end{cases}$$

At t_3: the body diodes of $Q^{(1)}{}_{r1}$ and $Q^{(2)}{}_{r2}$ turn on, both at zero voltage, and $v^{(i)}{}_{\rm cr1}$ and $v^{(i)}{}_{\rm cr2}$ become equal. Consequently, the circuit returns to the original state.

Since the integral of the current through C_o over one switching period at steady state equals to zero; $\int i_{\rm dr}(t)\,dt = V_o/R_Lf_s$. Using the boundary condition $i_r(t_1) = i_{\rm dr,peak}/2$, the following equation can be obtained as:

$$i_r(t_1) = V_o\sqrt{\frac{1}{2L_rR_Lf_s}}. \quad (16)$$

On the other hand, the integral of the current through $C^{(1)}{}_{r1}$ over one switching period at steady state equals to zero; $v^{(1)}{}_{\rm cr1}(t_0) = v^{(1)}{}_{\rm cr1}(t_3)$. Using the boundary condition $v^{(1)}{}_{\rm cr1}(t_1) = V_o$, the following equation can be obtained from

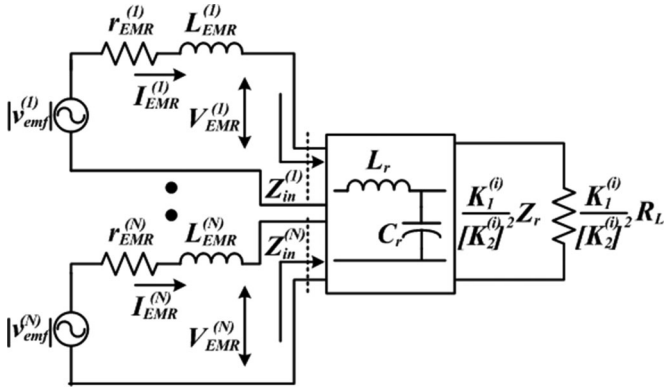

Fig. 6. Impedance network of an *N*-channel system.

(3), (4), (9), and (16).

$$V_o \ \left[1-\sqrt{\frac{\omega_r Z_r}{2R_L f_s}}\sin\omega_r(t_1-t_0)-\cos\omega_r(t_1-t_0)\right] = \frac{t_3-t_1}{NC_r}\sum_{i=1}^{N} I_{\mathrm{EMR}}^{(i)}. \tag{17}$$

By setting the transistor turn-on time $t_{\mathrm{on}} = t_1 - t_0 = 3T_r/4 = 3\pi/2\omega_r$ and $R_L >> Z_r$, V_{o} can be represented in terms of the sum of $I^{(i)}{}_{\mathrm{EMR}}$ as

$$V_o = \frac{t_{\mathrm{off}}}{NC_r}\sum_{i=1}^{N} I_{\mathrm{EMR}}^{(i)} \tag{18}$$

where $t_{\mathrm{off}} = t_3 - t_1 = T_s - t_{\mathrm{on}}$ is the turn-off time interval. By introducing the ratio of angular resonance frequency to switching frequency ($\gamma = f_r/f_s$) and the coefficient $\alpha = 4\gamma - 3$, (18) can be written as

$$V_o = \alpha\pi Z_r \sum_{i=1}^{N} I_{\mathrm{EMR}}^{(i)}. \tag{19}$$

The switching frequency (f_s) is slightly higher than the resonance frequency (f_r). When $R_L >> Z_r$, the converter can be considered as a current-controlled voltage-source. The impedance network of an *N*-channel system during one switching period is shown in Fig. 6. V_{o} is determined by the sum of the reed currents ($I^{(i)}{}_{\mathrm{EMR}}$), through setting the network impedance (Z_{r}) to a desired value. At the same Z_r and load condition, connecting more EMR generators results in a higher output voltage. Furthermore, the output voltage regulation can be achieved through real-time pulse frequency modulation (PFM).

III. Optimal Impedance Matching

To extract the maximum power from an *N*-channel system, it is necessary to acquire the equivalent input impedance of an *N*-input converter depicted in Fig. 6. In the case of a resistive load (R_L) comparable to Z_r, in one switching period, including R_L in V_o yields

$$\frac{V_o}{\sum_{i=1}^{N} I_{\mathrm{EMR}}^{(i)}} = \frac{\alpha\pi Z_r}{1+\sqrt{\pi Q_r \gamma}} \tag{20}$$

where $Q_r = Z_r/R_L$ denotes the quality factor. According to (20) and $V_o = I_o R_L$, the output-to-input current ratio can be represented as

$$\frac{I_o}{\sum_{i=1}^{N} I_{\mathrm{EMR}}^{(i)}} = \frac{\alpha\pi Q_r}{1+\sqrt{\pi Q_r \gamma}}. \tag{21}$$

In a vibration cycle, considering the conversion efficiency (η_{ff}), the generated power ($P^{(i)}{}_{\mathrm{EMR}}$) from each reed and the output power (P_o) of the converter should satisfy

$$\begin{cases} P_{\mathrm{EMR}}^{(i)} = V_{\mathrm{EMR}}^{(i)} I_{\mathrm{EMR}}^{(i)} = K_1^{(i)} \sum_{i=1}^{N} P_{\mathrm{EMR}}^{(i)} & (22) \\ I_{\mathrm{EMR}}^{(i)} = K_2^{(i)} \sum_{i=1}^{N} I_{\mathrm{EMR}}^{(i)} & (23) \\ P_o = V_o I_o = \eta_{ff} \sum_{i=1}^{N} P_{\mathrm{EMR}}^{(i)} & (24) \\ Z_{\mathrm{in}}^{(i)} = \dfrac{V_{\mathrm{EMR}}^{(i)}}{I_{\mathrm{EMR}}^{(i)}} = \dfrac{P_{\mathrm{EMR}}^{(i)}}{[I_{\mathrm{EMR}}^{(i)}]^2} & (25) \end{cases}$$

where $V_{\mathrm{EMR}}^{(i)}$ is the average terminal voltage of the ith reed during one switching period, $K_1^{(i)}$ is the percentage value of ith reed's generated power over total power, $K_2^{(i)}$ is the percentage value of ith reed's terminal current over total current, $Z^{(i)}{}_{\mathrm{in}}$ is the equivalent input impedance of the ith input connected to the ith reed. In a switching period, $K_1^{(i)}$ and $K_2^{(i)}$ can be assumed constant due to the assumption that the reed current ($I^{(i)}{}_{\mathrm{EMR}}$) and the reed power ($P^{(i)}{}_{\mathrm{EMR}}$) are constant. However, $K_1^{(i)}$ and $K_2^{(i)}$ are variable in a vibration cycle, since the reed current and the reed power oscillate at vibration frequency.

Based on (25), the equivalent input impedance connected to the ith reed can be expressed as

$$Z_{\mathrm{in}}^{(i)} = \frac{K_1^{(i)}}{[K_2^{(i)}]^2}\frac{(\alpha\pi Q_r)^2 R_L}{\eta_{ff}(1+\sqrt{\pi Q_r\gamma})^2} = \frac{K_1^{(i)}}{[K_2^{(i)}]^2} Z_{\mathrm{in}} \tag{26}$$

where Z_{in} is the equivalent input impedance of the ith input connected to the ith reed while other reeds are disconnected. $Z^{(i)}{}_{\mathrm{in}}$ is constant during a switching period; however, it changes in a vibration cycle due to the variable coefficients $K_1^{(i)}$ and $K_2^{(i)}$. The impedance network of an *N*-channel system during one vibration cycle is illustrated in Fig. 6. The characteristic impedance of the converter and load impedance are different for each reed, and they change during a vibration cycle. The total input power of the circuit is given by

$$\sum_{i=1}^{N} P_{\mathrm{EMR}}^{(i)} = \sum_{i=1}^{N} [I_{\mathrm{EMR}}^{(i)}]^2 Z_{\mathrm{in}}^{(i)} = Z_{\mathrm{in}} \sum_{j=1}^{N} K_1^{(j)} \left[\sum_{i=1}^{N} I_{\mathrm{EMR}}^{(i)}\right]^2 = Z_{\mathrm{in}}\left[\sum_{i=1}^{N} I_{\mathrm{EMR}}^{(i)}\right]^2. \tag{27}$$

According to the general model of EMR generators, the maximum power of the ith reed connected to the ith input can be extracted when the input impedance of the ith input equals to the optimal input impedance ($Z^{(i)}{}_{\mathrm{in}} = Z_{\mathrm{opt}}$). However, for an

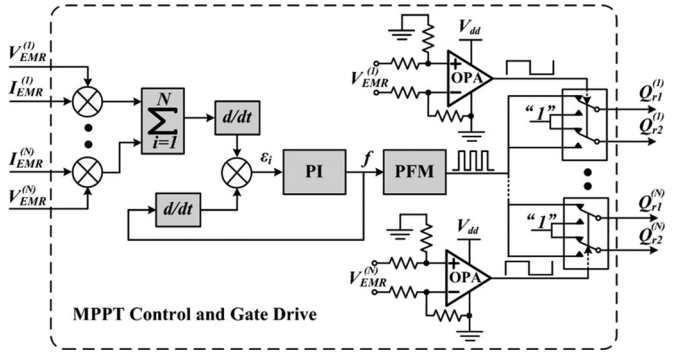

Fig. 7. Illustrative scheme of the MPPT control strategy and gate drive.

N-channel system connected to an *N*-input converter, the maximum power of the *N*-channel system is extracted as

$$P_{\mathrm{EMR,max}} = Z_{\mathrm{in}} \left[\sum_{i=1}^{N} I_{\mathrm{EMR}}^{(i)} \right]^2 \Bigg|_{Z_{\mathrm{in}} = Z^*_{\mathrm{opt}}} \tag{28}$$

where $Z^*{}_{\mathrm{opt}} \leq Z_{\mathrm{opt}}$. (28) reveals the fact that the total maximum power of an *N*-channel system is extracted through achieving optimal impedance matching of the *N*-input converter ($Z_{\mathrm{in}} = Z^*{}_{\mathrm{opt}}$) rather than optimal impedance matching of each input ($Z^{(i)}{}_{\mathrm{in}} = Z_{\mathrm{opt}}$). The optimal impedance can be acquired by setting characteristic impedance (Z_r) of *LC* network.

In addition to the impedance matching through *LC* network design, the input impedance can be further regulated in real time by PFM. Increasing the switching frequency (f_s) reduces the equivalent input impedance (Z_{in}). A closed-loop PI control is used to acquire the optimal switching frequency (f_{opt}) corresponding to Z_{opt}. f_s is increased when both derivations of the total input power and f_s have the same polarity; on the other hand, it is decreased when the derivation polarities of the total input power and f_s are different. The maximum power point tracking (MPPT) control and gate drive system is demonstrated in Fig. 7. Zero-crossing comparators are used to generate pulse signals synchronous with the reed vibration. Demultiplexer switches are controlled by pulse signals to produce MOSFET gating signals.

IV. Experimental Results

A 5 cm × 3 cm, six-input prototype of the proposed resonant converter, illustrated in Fig. 8, is fabricated for power conditioning of six EMR generators. Components and design parameters of the prototype PEI are listed in Table I.

A. PEI Design Specification

In order to achieve optimal impedance matching for a six-channel system, the characteristic impedance (Z_r) is set equal to 133 Ω. For a more powerful source, Z_r and Z_{in} can be reduced through either reducing the resonant inductance or increasing resonant capacitance. Moreover, the natural frequency (f_r) is set to 45 kHz with consideration of resonant losses and size miniaturization. Higher resonant frequency leads to smaller size of passive components; however, it results in higher resonant losses. The switching frequency (f_s) is chosen to be 48 kHz, slightly higher than f_r. The resonant inductor and resonant capacitors are determined as

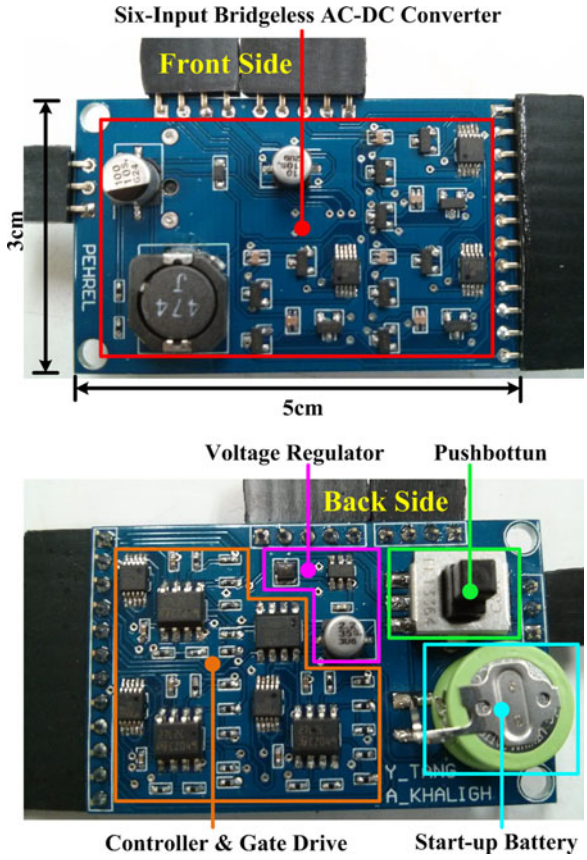

Fig. 8. Six-input standalone prototype of the proposed resonant ac–dc converter for a six-channel EMR-generator system.

TABLE I
Component Parameters of EMR Generator and PEI

Parameter	Description	Quantity	Part Number
	Power Converter		
Resonant capacitor ($C_{r1}{}^{(1)\sim(6)}$, $C_{r2}{}^{(1)\sim(6)}$)	2.2 nF, 50 V, Array	six	CKCM25×8R1H222M060AK
Resonant inductor (L_r)	470 μH, 0.62 A, 0.89 Ω	one	MSS1048-474KL
Output dc capacitor (C_o)	100 μF, 10 V	one	EEE-1AA101WR
Transistor ($Q_{r1}^{(1)\sim(6)}$, $Q_{r2}^{(1)\sim(6)}$)	20 V, 1.9 A, 63 mΩ	12	IRLML2030TRPBF
Diode (D_r)	20 V, 0.5 A, 0.3 V	one	DB2J20900L
	Control Board		
Microcontroller	3V, 144 μA, 2 PWM, 3 ADC	one	ATTINY13V-10SSU
OpAmp	0.04 V/μs, 3 V, 14 μA	three	TS27L2CDT
Resistor	100 kΩ	12	MCR01MRTJ104
Capacitor	1 nF, 10 V	six	C1005JB1H102K050BA

$$\begin{cases} L_r = \dfrac{Z_r}{2\pi f_r} & (29) \\ C_r = \dfrac{1}{4\pi N f_r Z_r}. & (30) \end{cases}$$

In order to reduce the resonant losses at low power, a 470-μH inductor with low dc resistance is selected as the resonant inductor (L_r, much smaller than the self-inductance of the EMR generator). 2.2-nF/50-V ceramic capacitor arrays are used as resonant capacitors. The MOSFETs with high compactness, fast

TABLE II
ELECTRICAL PERFORMANCES OF TESTBED

Parameter	Nominal Value
Power Amplifier	
Input frequency ($f_{\rm in}$)	20∼50 Hz
Open-circuit voltage ($v_{\rm emf}$)	0.5∼3 V (rms)
Terminal voltage ($V_{\rm EMR}$)	2.5∼7 V (peak)
Output power ($P_{\rm EMR}$)	1.8∼34 mW
EMR Generator	
Input frequency ($f_{\rm in}$)	15 Hz
Open-circuit voltage ($v_{\rm emf}$)	0.5∼2.5 V (rms)
Reed terminal voltage ($V_{\rm EMR}$)	2.5∼5 V (peak)
Output power ($P_{\rm EMR}$)	1∼4.5 mW
Power Converter	
Switching frequency (f_s)	48 kHz
Resonant frequency	45 kHz
Characteristic impedance	133 Ω
Output voltage	1.2∼5.5 V
Output power	1.5∼30 mW
Efficiency	85∼91%

transient response and low on-resistance are selected to reduce conduction losses. These MOSFETs have low gate charge and low gate voltage (as low as 2 V). Hence, the circuit can operate with low supply voltage, and will have low gating power dissipation as well as fast transient response. The rectifier diode (D_r) is selected based on the low forward voltage and low on-resistance. Low-power components are selected in the control board to enhance the standalone capability. ATTINY13V is used as the controller due to its low profile package, low power consumption and minimum required functions. Opamps and demultiplexer switches are adopted to detect the input polarity and provide gating signals.

B. Energy Harvesting Testbed

The prototype is tested with different sources to evaluate the operational performance at low power. The summary of circuit performance is listed in Table II. A 1-V dc source corresponding to 1-V EMF of the EMR generator is first applied to demonstrate the circuit's switching operation. A 1.5-mH inductor corresponding to the self-inductance of the EMR generator is placed in conjunction with each input. The experimental waveforms at 48-kHz switching frequency are presented in Fig. 9(a) and (b). High switching frequency can be achieved by tuning the network, illustrated in Fig. 9(c). According to the switching waveforms, the MOSFETs and the diode have ZVS turn-on and turn-off characteristics at the switching frequency close to the resonant frequency. A 2.4-V maximum output voltage is acquired through a 1-kΩ dc resistive load, with 94.4% dc–dc conversion efficiency.

A power amplifier circuit in conjunction with 1.5-mH inductors at each input is utilized to emulate the inductive ac sources. In this case, the overall input power is evenly split between six channels. The rms voltage of the power amplifier is set at 0.5∼3 V corresponding to the EMF voltage, $v_{\rm emf}$, of EMR generators. 20∼50-Hz ac frequency corresponding to low mechanical vibration frequency of EMR generator is selected to investigate the case of ambient energy harvesting. The measured output power varies from 1.5 to 30 mW at 20-Hz ac input power, as presented in Fig. 10(a) and (b), respectively. The converter shows good performance on rectification of a wide range

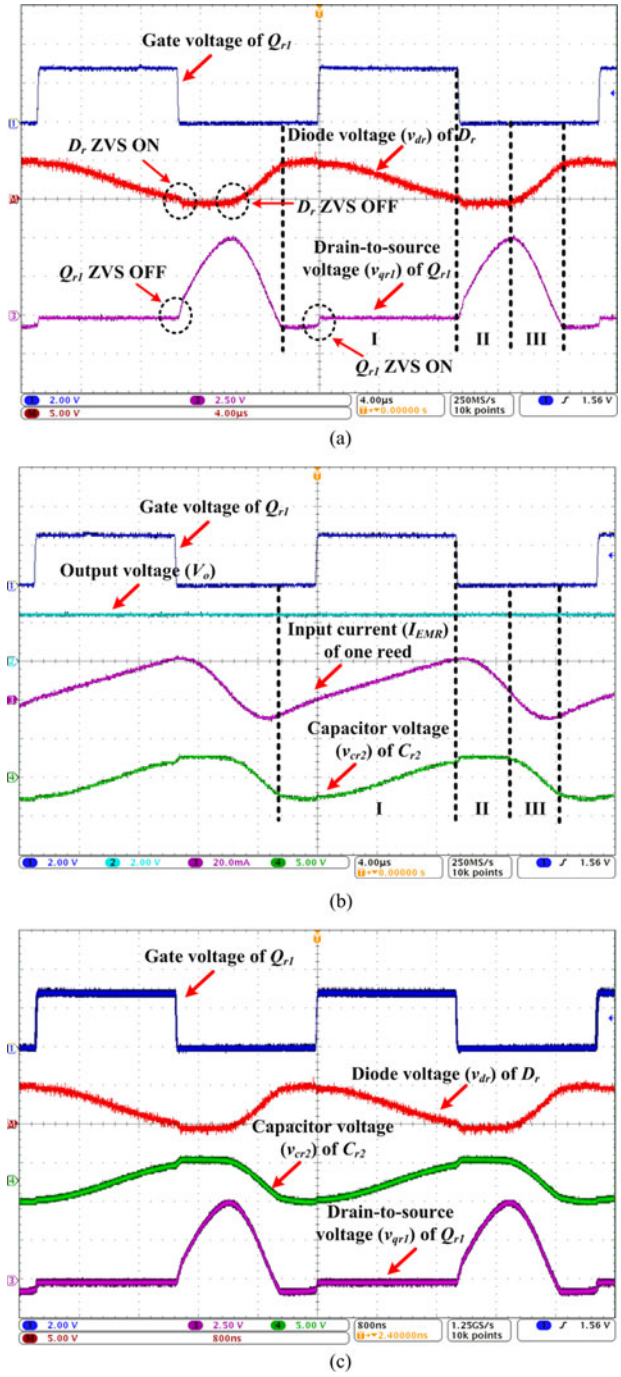

Fig. 9. Experimental waveforms of switching operation: $v_{\rm emf} = 1$V, $f_s =$ 48 kHz; x-axis: 4 μs/div; y-axis: (a) Ch1 = gate voltage of Q_{r1}, 2 V/div; Ch3 = drain-to-source voltage (v_{qr1}) of Q_{r1}, 2.5 V/div; ChM = diode voltage ($v_{\rm dr}$) of D_r, 5 V/div; and (b) Ch1 = gate voltage of Q_{r1}, 2 V/div; Ch2 = output voltage (V_o), 2 V/div; Ch3 = input current ($I_{\rm EMR}$) of one input, 20 mA/div; Ch4 = inductor voltage (v_r), 5 V/div; and (c) $f_s = 200$ kHz, Ch1 = gate voltage of Q_{r1}, 2 V/div; Ch3 = drain-to-source voltage (v_{qr1}) of Q_{r1}, 2.5 V/div; Ch4 = inductor voltage (v_r), 5 V/div; ChM = diode voltage ($v_{\rm dr}$) of $D_{\rm r}$, 5 V/div.

of EMF voltages (from 0.5 to 3 V). Furthermore, experimental waveforms with step change of input ac power and input ac frequency are illustrated in Fig. 11(a) and (b), respectively. The ac–dc conversion efficiency is above 80% even at very-low input voltage and power.

There are two types of losses: 1) power stage losses and 2) controller losses. Since the switching losses are eliminated

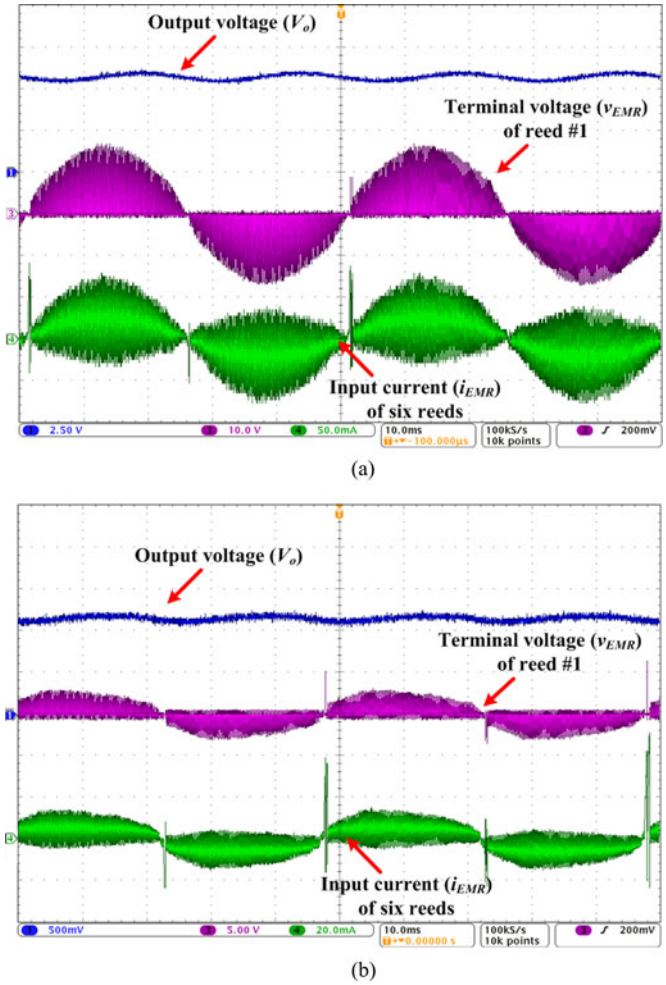

Fig. 10. Experimental waveforms of power amplifiers: $f_{\rm in} = 20$ Hz; x-axis: 10 ms/div; y-axis: (a) $v_{\rm emf} = 3$ $V_{\rm rms}$; Ch1 = output voltage (V_o), 2.5 V/div; Ch2 = terminal voltage ($v_{\rm EMR}$) of reed #1, 10 V/div; Ch3 = input current ($i_{\rm EMR}$) of six reeds, 50 mA/div; and (b) $v_{\rm emf} = 0.5$ $V_{\rm rms}$; Ch1 = output voltage (V_o), 0.5 V/div; Ch2 = terminal voltage ($v_{\rm EMR}$) of reed #1, 5 V/div; Ch3 = sum of the input currents ($i_{\rm EMR}$) of six reeds, 10 mA/div.

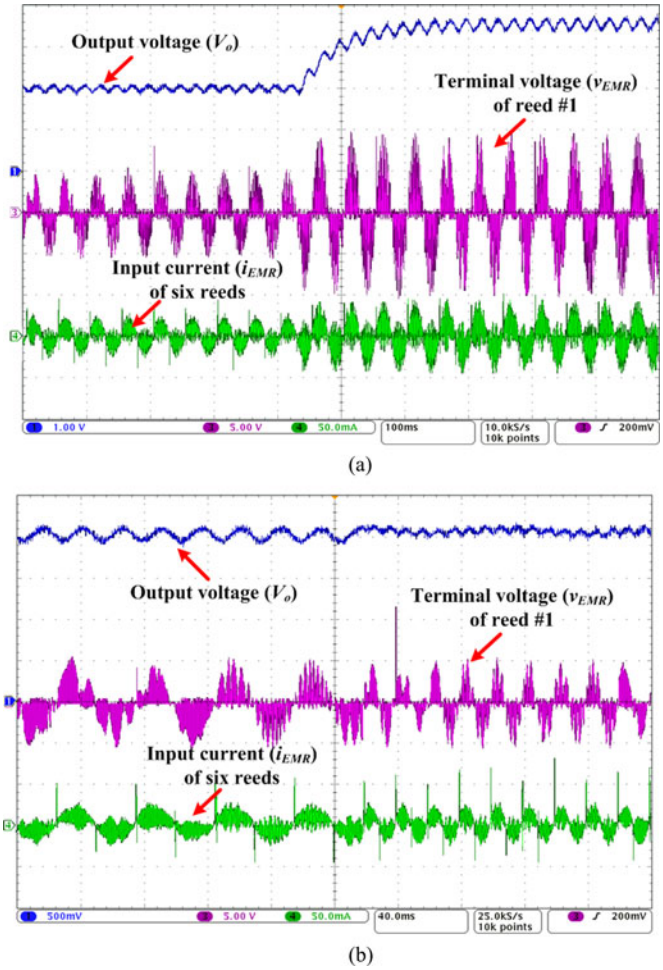

Fig. 11. Experimental waveforms of power amplifiers with step change: x-axis: 40 ms/div; y-axis: (a) $v_{\rm emf}$ = from 1 $V_{\rm rms}$ to 2 $V_{\rm rms}$; Ch1 = output voltage (V_o), 1 V/div; Ch2 = terminal voltage ($v_{\rm EMR}$) of reed #1, 5 V/div; Ch3 = input current ($i_{\rm EMR}$) of six reeds, 50 mA/div; and (b) $f_{\rm in}$ = from 20 to 50 Hz; Ch1 = output voltage (V_o), 0.5 V/div; Ch2 = terminal voltage ($v_{\rm EMR}$) of reed #1, 5 V/div; Ch3 = input current ($i_{\rm EMR}$) of six reeds, 50 mA/div.

through the resonant operation, the power stage losses can be categorized as the transistor conduction losses and the inductor losses. The controller stage losses include losses associate with the microcontroller, operational amplifiers and demultiplexer switches.

The conduction losses ($P_{\rm con}$), including transistor turn-on conduction losses (P_Q), inductor copper losses (P_{Lr}) and diode forward power losses ($P_{\rm dr}$), are represented as

$$P_{\rm con} = P_Q + P_{Lr} + P_{\rm dr} = \sum_{i=1}^{12} R_{Q,{\rm on}}^{(i)} \cdot [I_{Q,{\rm rms}}^{(i)}]^2 + R_{Lr} \cdot I_{Lr,{\rm rms}}^2 + V_{{\rm dr,fw}} \cdot I_{{\rm dr,avg}} \quad (31)$$

where $R_{Q,{\rm on}}^{(i)}$ is the drain-to-source on-state resistance of the transistors, $I^{(i)}{}_{Q,{\rm rms}}$ is RMS value of the transistor current, R_{Lr} is the coil resistance of the resonant inductor, $I_{Lr,{\rm rms}}$ is RMS value of the resonant inductor current, $V_{\rm dr,fw}$ is the forward voltage drop of the output diode, and $I_{\rm dr,avg}$ is the average value of the diode current. In addition, the inductor ferrite losses, composed of hysteresis loss ($P_{\rm hys}$) and eddy current loss ($P_{\rm eddy}$), can be expressed as

$$P_{\rm fer} = P_{\rm hys} + P_{\rm eddy} = K_h \cdot f_s \cdot B_{\rm max}^n + K_e \cdot f_s^2 \cdot B_{\rm max}^2 \quad (32)$$

TABLE III
POWER LOSS ESTIMATION OF PEI

Component	Power Loss	Loss Breakdown
Power Stage	*2.21 mW*	*55.8%*
Transistor ($P_Q^{(1)\sim(12)}$)	0.25 mW	6.3%
Diode ($P_{\rm dr}$)	0.96 mW	24.2%
Inductor coil (P_{Lr})	0.7 mW	17.7%
Inductor core ($P_{\rm fer}$)	0.3 mW	7.6%
Controller	*1.75 mW*	*44.2%*
Microcontroller	1.2 mW	30.3%
Opamp	0.126 mW	3.2%
Demultiplexer	0.18 mW	4.6%
Gating	0.2 mW	5.1%
Sensing resistor	0.04 mW	1.0%

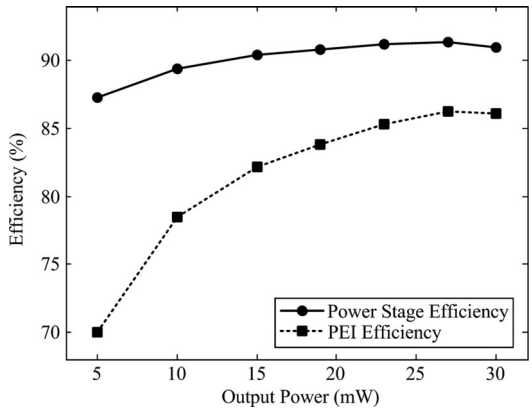

Fig. 12. Power conversion efficiency of the power stage and the entire PEI (including controller losses) at different output power.

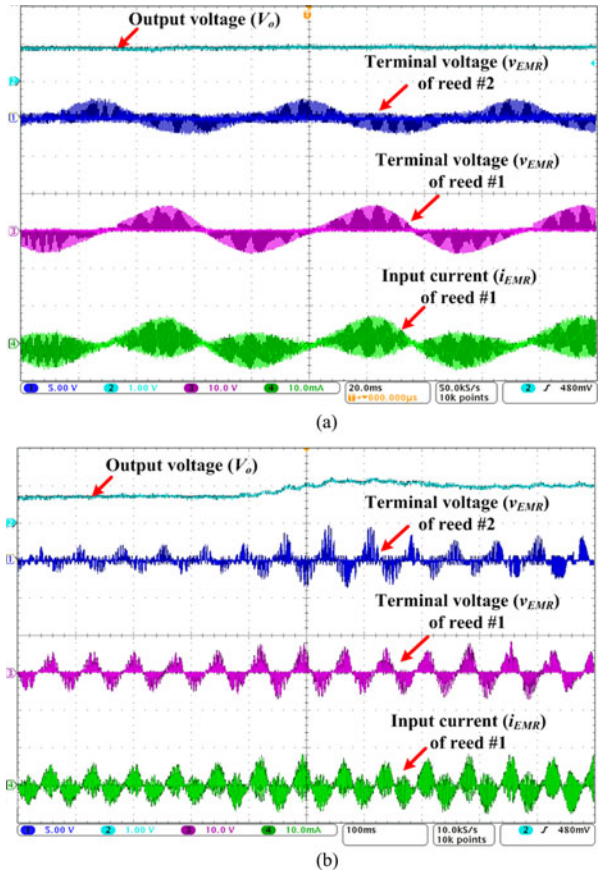

Fig. 13. Experimental waveforms of EMR generators: x-axis: (a) 20 ms/div; (b) 100 ms/div; y-axis: (a) constant wind speed; (b) wind speed step change; Ch1 = terminal voltage ($v_{\rm EMR}$) of reed #2, 5 V/div; Ch2 = output voltage (V_o), 1 V/div; Ch3 = terminal voltage ($v_{\rm EMR}$) of reed #1, 10 V/div; Ch4 = input current ($i_{\rm EMR}$) of reed #1, 10 mA/div.

where K_h and K_e are constants depending on magnetic material, f_s is the switching frequency, $B_{\max}$ is the maximum flux density, and n is a constant between 1.6 and 2.0.

The total loss of the converter at 23-mW output power is 3.96 mW. Table III summarizes the loss breakdown associated with each component. According to this table, power stage loss is 2.21 mW (55.8% of total loss) and controller loss is 1.75 mW (44.2% of total loss). The power conversion efficiency at different output power levels is presented in Fig. 12.

To verify the circuit performance with EMR generators, the prototype is connected to the six-channel wind panel. The reeds are driven by a low-speed fan and vibrate around 15 Hz. In this case, each reed generates a unique EMF and power. The terminal voltages ($v_{\rm EMR}$) of reed #1 and reed #2 and the input current ($i_{\rm EMR}$) of reed #1 are measured, as depicted in Fig. 13. Very low power (as low as 1 mW) can be extracted at low cutoff wind speed (as low as 3 m/s). The converter, connected to a 1-kΩ resistor, is capable of converting low EMFs (as low as 0.5 $V_{\rm rms}$) of six individual generators to a common dc output voltage (as high as 1.2 V), which make it suitable to charge a 1.2-V rechargeable battery.

V. Conclusion

This paper introduces a multiinput bridgeless resonant ac–dc converter suitable for efficient, low-voltage, low-power, ac–dc power conversion of multiple electromagnetic generators. The multiinput single-stage topology is capable of directly converting independent, low-amplitude, alternative voltages of EMR inductive generators to a stepped-up dc output voltage with relatively high efficiency. Low-frequency alternating voltages of EMR generators are first converted into a high-frequency alternating voltage through an *LC* network and then rectified into a dc output voltage through a soft-switched diode. Optimal electrical impedance matching is achieved through proper *LC* network design and PFM control to scavenge maximum power of EMR generators. In addition, high-frequency soft-switching increases the potential of size miniaturization without suffering from switching losses. The converter performance is verified through a 5 cm $\times$ 3 cm standalone prototype, which converts ac voltages of six-channel generators into a dc output voltage. A maximum PEI conversion efficiency of 86.3% is measured at 27-mW ac–dc power conversion. The topological concept, presented in this paper, can be adapted for rectification of any inductive voltage sources or electromagnetic energy-harvesting device.

References

[1] A. Khaligh, P. Zeng, and C. Zheng, "Kinetic energy harvesting using piezoelectric and electromagnetic technologies - State of the art," *IEEE Trans. Ind. Electron.*, vol. 57, no. 3, pp. 850–860, Mar. 2010.

[2] Altenera Technology Inc. (2014). [Online]. Available: http://altenera.com/products/.

[3] H. Jung, S. Lee, and D. Jang, "Feasibility study on a new energy harvesting electromagnetic device using aerodynamic instability," *IEEE Trans. Magn.*, vol. 45, no. 10, pp. 4376–4379, Oct. 2009.

[4] A. Bansal, D. A. Howey, and A. S. Holmes, "CM-scale air turbine and generator for energy harvesting from low-speed flows," in *Proc. Solid-State Sensors, Actuators Microsyst. Conf.*, Jun. 2009, pp. 529–532.

[5] D. Rancourt, A. Tabesh, and L. G. Fréchette, "Evaluation of centimeter-scale micro windmills: Aerodynamics and electromagnetic power generation," in *Proc. Power MEMS*, 2007, pp. 93–96.

[6] G. D. Szarka, B. H. Stark, and S. G. Burrow, "Review of power conditioning for kinetic energy harvesting systems," *IEEE Trans. Power Electron.*, vol. 27, no. 2, pp. 803–815, Feb. 2012.

[7] J. C. Farrarons, P. M. Català, A. S. Vela, M. P. Vidal, and J. Samitier, "Power-conditioning circuitry for a self-powered system based on micro PZT generators in a 0.13-μm low-voltage low-power technology," *IEEE Trans. Ind. Electron.*, vol. 55, no. 9, pp. 3249–3257, Sep. 2008.

[8] Y. Tang, C. Chen, A. Khaligh, I. Penskiy, and S. Bergbreiter, "An ultra-compact dual-stage converter for driving electrostatic actuators in mobile microrobots," *IEEE Trans. Power Electron.*, vol. 29, no. 6, pp. 2991–3000, Jun. 2014.
[9] A. Tabesh and L. G. Fréchette, "A low-power stand-alone adaptive circuit for harvesting energy from a piezoelectric micropower generator," *IEEE Trans. Ind. Electron.*, vol. 57, no. 3, pp. 840–849, Mar. 2010.
[10] E. Lefeuvre, D. Audigier, C. Richard, and D. Guyomar, "Buck-boost converter for sensorless power optimization of piezoelectric energy harvester," *IEEE Trans. Power Electron.*, vol. 22, no. 5, pp. 2018–2025, Sep. 2007.
[11] C. Chen, Y. Tang, A. Khaligh, and R. W. Newcomb, "A low-power and high-gain converter for driving dielectric elastomer actuators," in *Proc. IEEE Appl. Power Electron. Conf. Expo.*, Mar. 2013, pp. 2755–2760.
[12] G. K. Ottman, H. F. Hofmann, and G. A. Lesieutre, "Optimized piezoelectric energy harvesting circuit using step-down converter in discontinuous conduction mode," *IEEE Trans. Power Electron.*, vol. 18, no. 2, pp. 696–703, Mar. 2003.
[13] A. Badel, A. Benayad, E. Lefeuvre, L. Lebrun, C. Richard, and D. Guyomar, "Single crystals and nonlinear process for outstanding vibration-powered electrical generators," *IEEE Trans. Ultrason., Ferroelectr., Freq. Control*, vol. 53, no. 4, pp. 673–684, Apr. 2006.
[14] V. Vijayan and K. Vinida, "A review of ac-dc boost converters for low voltage energy harvesting," *Int. J. Emerging Tech. Adv. Eng.*, vol. 4, no. 6, pp. 841–846, Jun. 2014.
[15] Y. Tang and A. Khaligh, "Miniaturized bridgeless high-frequency resonant ac-dc step-up/step-down converters," *IEEE Trans. Power Electron.*, vol. 29, no. 12, pp. 6518–6533, Dec. 2014.
[16] Y. Tang and A. Khaligh, "A novel bridgeless high-frequency resonant ac-dc converter," in *Proc. IEEE Appl. Power Electron. Conf. Expo.*, Mar. 2014, pp. 125–130.
[17] T. T. Le, J. Han, A. V. Jouanne, K. Mayaram, and T. S. Fiez, "Piezoelectric micro-power generation interface circuits," *IEEE J. Solid-State Circuits*, vol. 41, no. 6, pp. 1411–1420, Jun. 2006.
[18] J. C. Farrarons, P. M. Català, A. S. Vela, M. P. Vidal, and J. Samitier, "Power-conditioning circuitry for a self-powered system based on micro PZT generators in a 0.13-μm low-voltage low-power technology," *IEEE Trans. Ind. Electron.*, vol. 55, no. 9, pp. 3249–3257, Sep. 2008.
[19] G. Bawa and M. Ghovanloo, "Analysis, design, and implementation of a high-efficiency full-wave rectifier in standard CMOS technology," *IEEE J. Analog Integr. Circuits Signal Process.*, vol. 60, no. 1, pp. 71–81, Aug. 2009.
[20] J. C. Salmon, "Circuit topologies for single-phase voltage-doubler boost rectifiers," *IEEE Trans. Power Electron.*, vol. 8, no. 4, pp. 521–529, Oct. 1993.
[21] P. D. Mitcheson, T. C. Green, and E. M. Yeatman, "Power processing circuits for electromagnetic, electrostatic and piezoelectric inertial energy scavengers," *Microsyst. Technol.*, vol. 13, pp. 1629–1635, Jul. 2007.
[22] H. Wang, Y. Tang, and A. Khaligh, "A bridgeless boost rectifier for low voltage energy harvesting applications," *IEEE Trans. Power Electron.*, vol. 28, no. 11, pp. 5206–5214, Jan. 2013.
[23] N. Mohan, T. M. Undeland, and W. P. Robbins, *Power Electronics: Converters, Applications, and Design*. New York, NY, USA: Wiley, 1995.
[24] F. C. Lee, "High-frequency quasi-resonant converter technologies," *Proc. IEEE*, vol. 76, no. 4, pp. 377–390, Apr. 1988.
[25] I. Aksoy, H. Bodur, and A. F. Bakan, "A new ZVT-ZCT-PWM dc-dc converter," *IEEE Trans. Power Electron.*, vol. 25, no. 8, pp. 2093–2105, Aug. 2010.
[26] W. Tabisz and F. C. Lee, "Zero-voltage-switching multiresonant technique - A novel approach to improve performance of high-frequency quasiresonant converters," *IEEE Trans. Power Electron.*, vol. 4, no. 4, pp. 450–458, Oct. 1989.
[27] D. Guyomar, A. Badel, E. Lefeuvre, and C. Richard, "Toward energy harvesting using active materials and conversion improvement by nonlinear processing," *IEEE Trans. Ultrason., Ferroelectr. Freq. Control*, vol. 52, no. 4, pp. 584–595, Apr. 2005.
[28] L. Garbuio, M. Lallart, D. Guyomar, C. Richard, and D. Audigier, "Mechanical energy harvester with ultralow threshold rectification based on SSHI nonlinear technique," *IEEE Trans. Ind. Electron.*, vol. 56, no. 4, pp. 1048–1056, Apr. 2009.
[29] E. Lefeuvre, A. Badel, C. Richard, and D. Guyomar, "Piezoelectric energy harvesting device optimization by synchronous electric charge extraction," *J. Intell. Mater. Syst. Struct.*, vol. 16, no. 10, pp. 865–876, 2005.
[30] M. Lallart, C. Richard, L. Garbuio, L. Petit, and D. Guyomar, "High efficiency, wide load bandwidth piezoelectric energy scavenging by a hybrid nonlinear approach," *Sensors Actuators A: Phys.*, vol. 165, no. 2, pp. 294–302, 2011.
[31] J. Hu, A. D. Sagneri, J. M. Rivas, Y. Han, S. M. Davis, and D. J. Perreault, "High-frequency resonant SEPIC converter with wide input and output voltage ranges," *IEEE Trans. Power Electron.*, vol. 27, no. 1, pp. 189–200, Jan. 2012.
[32] S. J. Roundy, "Energy scavenging for wireless sensor nodes with a focus on vibration to electricity conversion," Ph.D. dissertation, Dept. Mech. Eng., Univ. California, Berkeley, CA, USA, 2003.
[33] M. El-hami, P. Glynne-Jones, N. M. White, M. Hill, S. Beeby, E. James, A. D. Brown, and J. N. Ross, "Design and fabrication of a new vibration-based electromechanical power generator," *Sensors Actuators A: Phys.*, vol. 92, no. 1–3, pp. 335–342, Aug. 2001.

Yichao Tang (S'12) received the B.S. degree from Shanghai Jiaotong University, Shanghai, China, in 2009, and the M.S. degree from the Illinois Institute of Technology, Chicago, IL, USA, in 2011, both in electrical engineering. He is currently working toward the Ph.D. degree at the Electrical and Computer Engineering Department, University of Maryland, College Park, MD, USA.

Since he joined the Power Electronics, Energy Harvesting and Renewable Energies Laboratory in August 2011, he has been working on developing miniaturized power electronic interfaces for low-voltage low-power energy harvesting systems and for driving high-voltage actuators in mobile microrobotic insects, as well as integrated level-two and level-three onboard chargers for plug-in electric vehicles (PEV). He is the author/coauthor of 11 refereed journal/conference papers and two provisional patents. His research interests include modeling, analysis, design and control of ac–dc, dc–dc and dc–ac power electronic converters, energy harvesting from environmental sources, renewable energies, power autonomy of mobile microrobots, electric chargers for EV and PEV, as well as power conditioning systems for more electric aircraft and shipboard power systems.

Alireza Khaligh (S'04–M'06–SM'09) is the Director of Power Electronics, Energy Harvesting and Renewable Energies Laboratory, Electrical and Computer Engineering (ECE) Department, and the Institute for Systems Research (ISR), University of Maryland, College Park (UMCP), MD, USA. Prior to UMCP, he was a Postdoctoral Research Associate at the Grainger Center for Electric Machinery and Electromechanics, University of Illinois at Urbana-Champaign, Urbana, IL, USA, and also an Assistant Professor at the Illinois Institute of Technology (IIT), Chicago, IL. He is an author/coauthor of more than 130 journals and conference papers. His major research interests include modeling, analysis, design, and control of power electronic converters for transportation electrification, renewable energies, energy harvesting, and microrobotics.

Dr. Khaligh is a recipient of various awards and recognitions including the 2015 Inaugural ISR Junior Faculty Fellowship, the 2013 George Corcoran Memorial Award from the ECE Department of the University of Maryland, 2013 Best Vehicular Electronics Paper Award from IEEE Vehicular Technology Society, 2010 Ralph R. Teetor Educational Award from the Society of Automotive Engineers, and the 2009 Armour College of Engineering Excellence in Teaching Award from IIT. He was the Program Chair of the 2015 IEEE Applied Power Electronics Conference and Expo (APEC), the Assistant Program Chair of the 2014 IEEE APEC, the General Chair of the 2013 IEEE Transportation Electrification Conference and Expo, the Grants and Awards Chair of the 2012–2013 APEC, and the Program Chair of the 2011 IEEE Vehicle Power and Propulsion Conference. He is an Editor of the IEEE TRANSACTIONS ON VEHICULAR TECHNOLOGY, and an Associate Editor for the IEEE TRANSACTIONS ON TRANSPORTATION ELECTRIFICATION. He was a Guest Associate Editor for the Special Issue of the IEEE TRANSACTIONS ON POWER ELECTRONICS ON TRANSPORTATION ELECTRIFICATION AND VEHICLE SYSTEMS, a Guest Editor for the Special Section of the IEEE TRANSACTIONS ON VEHICULAR TECHNOLOGY ON SUSTAINABLE TRANSPORTATION SYSTEMS, and a Guest Editor for the Special Section of the IEEE TRANSACTIONS ON INDUSTRIAL ELECTRONICS ON ENERGY HARVESTING. He is the General Chair of the 2016 IEEE Applied Power Electronic Conference and Expo, *the most premier conference in applied power electronics*. He is a Distinguished Lecturer of the IEEE Vehicular Technology Society.